2020

Isogeometric analysis of ice accretion on wind turbine blades

Emily L. Johnson
Iowa State University, johnsel@iastate.edu

Ming-Chen Hsu
Iowa State University, jmchsu@iastate.edu

Isogeometric analysis of ice accretion on wind turbine blades

Abstract

For wind turbines operating in cold weather conditions, ice accretion is an established issue that remains an obstacle in effective turbine operation. While the aerodynamic performance of wind turbine blades with ice accretion has received considerable research attention, few studies have investigated the structural impact of blade ice accretion. This work proposes an adaptable projection-based method to superimpose complex ice configurations onto a baseline structure. The proposed approach provides an efficient methodology to include ice accretion in the high fidelity isogeometric shell analysis of a realistic wind turbine blade. Linear vibration and nonlinear deflection analyses of the blade are performed for various ice configurations to demonstrate the impact of different ice accretion distributions on structural performance. These analyses indicate decreases in the blade natural frequencies and deflection under icing conditions. Such ice-induced changes clearly reveal the need for structural design consideration for turbines operating under icing conditions.

Keywords

wind turbine blades, ice accretion, isogeometric analysis, laminated plates, thin composite shells

Disciplines

Computer-Aided Engineering and Design | Energy Systems | Mechanical Engineering | Structures and Materials

Comments

This is a pre-print of the article Johnson, Emily L., and Ming-Chen Hsu. "Isogeometric analysis of ice accretion on wind turbine blades." (2020). Posted with permission.

Computational Mechanics manuscript No.
(will be inserted by the editor)

Isogeometric analysis of ice accretion on wind turbine blades

Emily L. Johnson · Ming-Chen Hsu

The final publication is available at Springer via https://doi.org/10.1007/s00466-020-01852-y

Abstract For wind turbines operating in cold weather conditions, ice accretion is an established issue that remains an obstacle in effective turbine operation. While the aerodynamic performance of wind turbine blades with ice accretion has received considerable research attention, few studies have investigated the structural impact of blade ice accretion. This work proposes an adaptable projection-based method to superimpose complex ice configurations onto a baseline structure. The proposed approach provides an efficient methodology to include ice accretion in the high-fidelity isogeometric shell analysis of a realistic wind turbine blade. Linear vibration and nonlinear deflection analyses of the blade are performed for various ice configurations to demonstrate the impact of different ice accretion distributions on structural performance. These analyses indicate decreases in the blade natural frequencies and deflection under icing conditions. Such ice-induced changes clearly reveal the need for structural design consideration for turbines operating under icing conditions.

Keywords wind turbine blades · ice accretion · isogeometric analysis · laminated plates · thin composite shells

1 Introduction

Ice accretion on wind turbines is a well-known phenomenon that remains an issue for effective turbine operation in cold climates. Performance losses due to the incidence of icing are a commonly recognized and accepted concern in cold weather conditions that may lead to significant annual energy losses [1]. Wind turbine blade ice accretion, which occurs primarily near the leading edge, has demonstrated negative effects on blade performance, including reduced power outputs, surface erosion, and sudden blade failures and damage [2]. The aerodynamic impact of ice accretion, particularly related to changes in the airfoil and blade geometries due to ice formation, has been widely studied in correlation with wind turbine performance and power outputs [3–14]. A number of recent studies have also experimentally investigated the progression of ice accretion on wind turbine airfoils, including changes in the shape, distribution, and properties of ice that occur during this process [15, 16]. Despite the wide variety of investigations related to the aerodynamic effects of ice on wind turbine blades, studies on the structural impact of ice accretion have remained relatively limited.

A few prior studies have used experimental and numerical models to investigate the structural impacts of ice accretion on the aeroelastic behavior of blades [17, 18]. A previous numerical investigation focused on examining the impact of increased blade mass due to ice accretion [19]. Other work studied the effects of increased mass and load on the dynamic structural performance of wind turbine blades with ice accretion by incorporating aeroelastic equations [20] and reduced order beam modeling approaches [21] coupled with 2D computational fluid dynamics (CFD) simulations of the airfoil aerodynamics. These studies have indicated overall decreases in the aeroelastic natural frequencies of the blade due to the added mass and increased blade loads under icing conditions. However, to our knowledge, a high-fidelity model that directly considers the ice geometry and distributions has not been previously proposed to accurately model ice accretion on a realistic wind turbine blade.

In this work, we propose a novel approach for isogeometric analysis (IGA) of ice accretion on wind turbine blades. IGA was first introduced by Hughes et al. [22]

E.L. Johnson (✉) · M.-C. Hsu
Department of Mechanical Engineering, Iowa State University,
2043 Black Engineering, Ames, IA 50011, USA
E-mail: johnsel@iastate.edu (ELJ), jmchsu@iastate.edu (MCH)

to directly utilize the parameterizations within computer-aided design (CAD) models as finite element basis functions, which seamlessly integrates the design and analysis processes. It has since been used to solve the most challenging science and engineering applications [23–39]. For thin structures, isogeometric shells [40–57] have been previously demonstrated as an effective method for the analysis of complex problems [58–82], including the analysis of composites [83–92]. Isogeometric shells have also been effectively applied to wind turbine structural [93–97] and fluid–structure interaction [83, 98–105] analysis.

Here, we propose a simple, efficient projection-based approach to model ice accretion on isogeometric Kirchhoff–Love shells [40]. Due to the complex and dynamic nature of ice formation, this method provides a suitable approach that superimposes the ice geometry onto the baseline structure, which enables adaptable modeling of different intricate ice shapes without altering the underlying geometry and patch configurations. This projection-based method is then combined with the principle of classical laminated plate theory [106] to include the ice as an additional layer in the composite shell. The effectiveness of the proposed approach for modeling ice accretion in high-fidelity isogeometric shell analysis is demonstrated using a realistic 5 MW wind turbine blade. Using the developed procedure, this work investigates the impact of different ice configurations on the linear vibration and nonlinear deflection properties of the blade.

This paper is organized as follows. Section 2 outlines the isogeometric Kirchhoff–Love shell formulations, penalty coupling methods, and ice material and geometry modeling approaches. In Section 3, the proposed ice modeling methods are applied to the NREL/SNL 5 MW wind turbine blade to study the structural impact of ice accretion. Finally, Section 4 presents the conclusions from the study and the importance of the presented approaches for the design and analysis of realistic wind turbine blades.

2 Computational methods

2.1 Isogeometric analysis of thin-shell composites

Isogeometric Kirchhoff–Love thin shell analysis, which was first proposed by Kiendl et al. [40], has become a commonly used shell formulation that is effective for analyzing composite shells [83–88] and modeling wind turbine blade structures [94–97]. In the isogeometric Kirchhoff–Love shell theory, the Green–Lagrange strain tensor, $\mathbf{E}$, is expressed as a linear combination of the membrane strain tensor, $\boldsymbol{\varepsilon}$, and curvature change tensor, $\boldsymbol{\kappa}$, at the shell midsurface:

$$\mathbf{E} = \boldsymbol{\varepsilon} + \xi_3 \boldsymbol{\kappa} \,, \tag{1}$$

where ξ_3 is the through-thickness coordinate. This work assumes linear elastic material behavior, which corresponds to a St. Venant–Kirchhoff material model in which the stress–strain relationship is defined as

$$\mathbf{S} = \mathbb{C}\mathbf{E} \,, \tag{2}$$

where $\mathbf{S}$ is a second Piola–Kirchhoff stress tensor and $\mathbb{C}$ is a constitutive material tensor. The structural formulation is defined using the principle of virtual work as

$$\delta W^{\text{int}} - \delta W^{\text{ext}} = 0 \,, \tag{3}$$

where

$$\begin{aligned} \delta W^{\text{int}} &= \int_{\mathcal{S}} \int_{\xi_3} \delta\mathbf{E} : \mathbf{S} \, \mathrm{d}\xi_3 \mathrm{d}\mathcal{S} \\ &= \int_{\mathcal{S}} \delta\boldsymbol{\varepsilon} : (\mathbb{A}\boldsymbol{\varepsilon} + \mathbb{B}\boldsymbol{\kappa}) \, \mathrm{d}\mathcal{S} + \int_{\mathcal{S}} \delta\boldsymbol{\kappa} : (\mathbb{B}\boldsymbol{\varepsilon} + \mathbb{D}\boldsymbol{\kappa}) \, \mathrm{d}\mathcal{S} \,, \end{aligned} \tag{4}$$

and

$$\delta W^{\text{ext}} = \int_{\mathcal{S}} \delta\mathbf{u} \cdot \rho \, t \, \mathbf{f} \, \mathrm{d}\mathcal{S} + \int_{\mathcal{S}} \delta\mathbf{u} \cdot \mathbf{h} \, \mathrm{d}\mathcal{S} \,. \tag{5}$$

Here, δ denotes the variation with respect to the virtual displacement variable $\delta\mathbf{u}$, $\mathcal{S}$ denotes the shell midsurface in the reference configuration, ρ is the weighted average density through the shell thickness, t is the shell thickness, $\mathbf{f}$ indicates the body force per unit mass, $\mathbf{h}$ indicates the surface traction, and $\mathbb{A}$, $\mathbb{B}$, and $\mathbb{D}$ are the homogenized extensional (membrane), coupling, and bending stiffness tensors, respectively, which are defined as

$$\mathbb{A} = \int_{-t/2}^{t/2} \mathbb{C} \, \mathrm{d}\xi_3 = \sum_{k=1}^{n} \mathbb{C}_k t_k \,, \tag{6}$$

$$\mathbb{B} = \int_{-t/2}^{t/2} \xi_3 \mathbb{C} \, \mathrm{d}\xi_3 = \sum_{k=1}^{n} \mathbb{C}_k t_k z_k \,, \tag{7}$$

$$\mathbb{D} = \int_{-t/2}^{t/2} \xi_3^2 \mathbb{C} \, \mathrm{d}\xi_3 = \sum_{k=1}^{n} \mathbb{C}_k \left(t_k z_k^2 + \frac{t_k^3}{12} \right) \,, \tag{8}$$

based on the classical laminated plate theory [106]. In the above, n is the total number of composite piles, t_k is the thickness of the kth ply, and z_k is the distance from the centroid of the kth ply to the midplane of the laminate, as shown in Figure 1. In this work, all the tensors are written with respect to the local Cartesian basis; the local Cartesian basis is oriented on the first covariant base vector of the midsurface, which is aligned with the first parametric direction of the nonuniform rational B-spline (NURBS) surface.

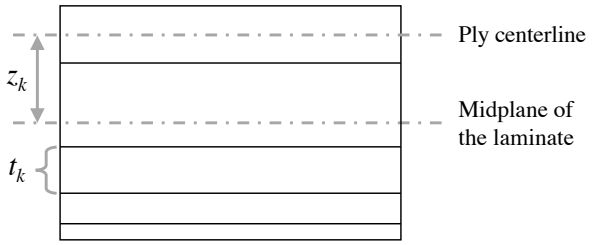

Fig. 1: Composite ply layup for a nonuniform and nonsymmetric laminated plate.

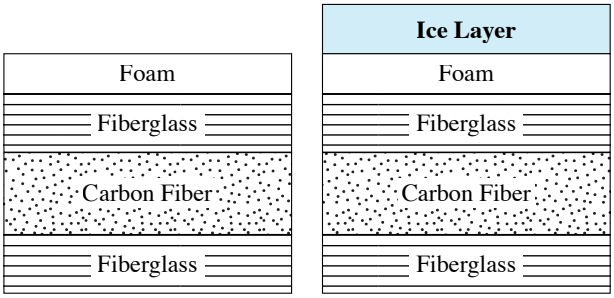

Fig. 2: Ice accretion on a thin-shell laminated plate.

2.2 Coupling of surface patches with matching or nonmatching discretization

Despite the many advantages offered by the isogeometric Kirchhoff–Love approach, C^1-continuous approximation functions are required to accommodate the second order derivatives in the variational governing equations [107]. Complex structures often comprise many NURBS surfaces that have C^0 or even C^{-1} continuity between patches. These conditions occur frequently in wind turbine blade modeling because it is not possible to model the shear webs and the outer surface of the blade with a single NURBS surface. To accommodate the geometric complexity of these structures, a penalty-based patch coupling approach was recently proposed to couple interfaces that have matching or nonmatching discretization [96]. Here we provide a summary.

For an interface between two surface patches, $\mathcal{S}^{\mathrm{A}}$ and $\mathcal{S}^{\mathrm{B}}$, with nonconforming discretization, two separate penalty energies are defined to constrain the displacements and rotations at the interface. The displacement penalty virtual work is defined as

$$\delta W^{\mathrm{pd}} = \int_{\mathcal{L}^{\mathrm{AB}}} \alpha_{\mathrm{d}} \left(\delta \mathbf{u}^{\mathrm{A}} - \delta \mathbf{u}^{\mathrm{B}}\right) \cdot \left(\mathbf{u}^{\mathrm{A}} - \mathbf{u}^{\mathrm{B}}\right) \mathrm{d}\mathcal{L} \,, \tag{9}$$

where $\mathcal{L}^{\mathrm{AB}}$ denotes the patch interface, $\mathbf{u}^{\mathrm{A}}$ and $\mathbf{u}^{\mathrm{B}}$ are the displacements of the corresponding points on surface patches $\mathcal{S}^{\mathrm{A}}$ and $\mathcal{S}^{\mathrm{B}}$, respectively, and α_{d} is a penalty parameter. For the rotational continuity between the two surfaces, the rotational penalty virtual work is defined as

$$\begin{aligned}\delta W^{\mathrm{pr}} = \int_{\mathcal{L}^{\mathrm{AB}}} \alpha_{\mathrm{r}} \left(\left(\delta \cos\phi - \delta \cos\phi_0\right)\left(\cos\phi - \cos\phi_0\right)\right. \\ \left. + \left(\delta \sin\phi - \delta \sin\phi_0\right)\left(\sin\phi - \sin\phi_0\right)\right) \mathrm{d}\mathcal{L} \,,\end{aligned} \tag{10}$$

where ϕ_0 and ϕ are the angles between the surfaces in the deformed and undeformed configurations, respectively, and α_{r} is a penalty parameter. The virtual work formulation, Eq. (3), is then restated as

$$\delta W^{\mathrm{int}} + \delta W^{\mathrm{pd}} + \delta W^{\mathrm{pr}} - \delta W^{\mathrm{ext}} = 0 \,. \tag{11}$$

To eliminate one of the inherent issues of penalty methods, the choice of penalty parameters should be problem-independent. An ideal penalty formulation should scale in a dimensionally consistent manner with the geometric and material properties of the problem to satisfy the penalty constraint at an appropriate level for the specified problem. In our recent work [96], we proposed a formulation to link the two penalty parameters, α_{d} and α_{r}, to a single dimensionless parameter, α, through the following definitions:

$$\alpha_{\mathrm{d}} = \alpha \frac{\min(\max_{i,j}(A^{\mathrm{A}}_{ij}), \max_{i,j}(A^{\mathrm{B}}_{ij}))}{(h^{\mathrm{A}} + h^{\mathrm{B}})/2} \,, \tag{12}$$

$$\alpha_{\mathrm{r}} = \alpha \frac{\min(\max_{i,j}(D^{\mathrm{A}}_{ij}), \max_{i,j}(D^{\mathrm{B}}_{ij}))}{(h^{\mathrm{A}} + h^{\mathrm{B}})/2} \,, \tag{13}$$

for $i = 1, 2$ and $j = 1, 2$, where A^{A}_{ij} and A^{B}_{ij} are the elements of local extensional stiffness matrices on surfaces $\mathcal{S}^{\mathrm{A}}$ and $\mathcal{S}^{\mathrm{B}}$, respectively, D^{A}_{ij} and D^{B}_{ij} are the elements of local bending stiffness matrices, and h^{A} and h^{B} are the length of the local elements in the direction most parallel to the penalty curve $\mathcal{L}^{\mathrm{AB}}$. As demonstrated in Herrema et al. [96], this formulation works effectively for a wide range of shell problems, including blade analysis, using a dimensionless penalty parameter of $\alpha = 10^3$.

2.3 Ice accretion modeling on thin-shell composites

To model the ice accumulation on the surface of the baseline composite, the ice is defined as an isotropic, elastic material [108] that is considered as an additional top layer in the definition of the composite layup, as shown in Figure 2. This approach assumes that the added ice layer thickness maintains the thin-shell assumption, which is a reasonable assumption for many types of ice accretion on wind turbine blades [2, Chap. 3]. The ice layer can then be considered as another ply in the laminated plate that is homogenized within the $\mathbb{A}$, $\mathbb{B}$, and $\mathbb{D}$ stiffness matrices as

$$\mathbb{A} = \sum_{k=1}^{n} \mathbb{C}_k t_k + \mathbb{C}_{\mathrm{ice}} t_{\mathrm{ice}} \,, \tag{14}$$

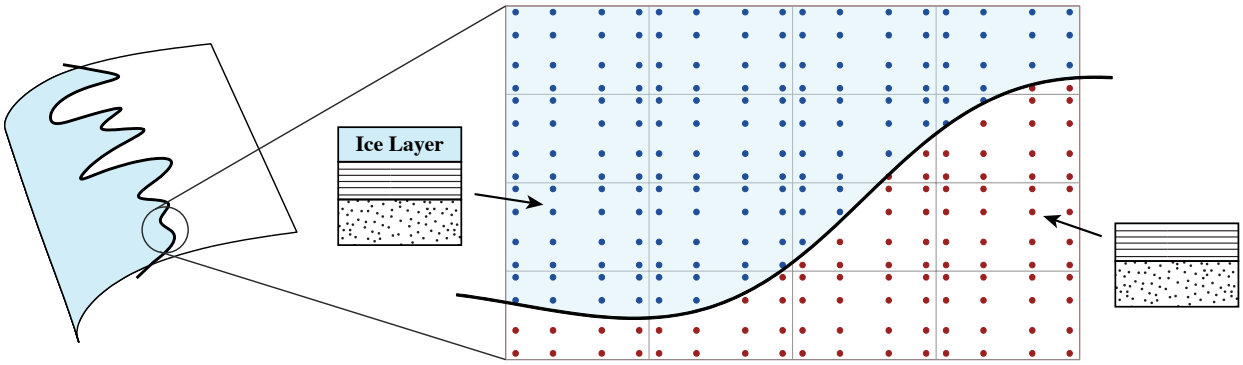

Fig. 3: Projection of the ice shape to the baseline geometry model.

$$\mathbb{B} = \sum_{k=1}^{n} \mathbb{C}_k t_k z_k + \mathbb{C}_{\text{ice}} t_{\text{ice}} z_{\text{ice}} \,, \tag{15}$$

$$\mathbb{D} = \sum_{k=1}^{n} \mathbb{C}_k \left(t_k z_k^2 + \frac{t_k^3}{12} \right) + \mathbb{C}_{\text{ice}} \left(t_{\text{ice}} z_{\text{ice}}^2 + \frac{t_{\text{ice}}^3}{12} \right) , \tag{16}$$

where $\mathbb{C}_{\text{ice}}$ is the constitutive material tensor of the ice, t_{ice} is the thickness of the ice layer, and z_{ice} is the distance from the centroid of the ice layer to the midplane of the laminate without ice. Note that this definition ensures that adding the ice layer does not change the location of the shell midplane. This formulation avoids redefining the shell midplane for the baseline composite when adding the ice layer, which provides a consistent approach to consider the dynamic and evolving nature of ice accretion. According to the classical laminated plate theory, the approach proposed here also assumes that the ice remains fully intact and adhered to the baseline surface as a layer in the composite shell.

A realistic definition of complex ice geometries requires an adaptable description of the ice profile, which may include configurations that are intricate and dynamically evolving. To accommodate such geometric complexity, this work proposes a flexible, projection-based definition that superimposes the ice regions onto the baseline model. This approach captures any possible geometric variability of the ice accretion, including spatial and temporal variations. Considering that it may be impractical to introduce significant variation in a given model with specified geometry and material definitions, this projection-based method provides a versatile ice definition that does not require modifying the baseline CAD geometries or NURBS patch structure. Using this method, as shown in Figure 3, the defined ice profile is projected to the baseline surface to divide it into subsections. Each surface integration point within a particular subsection is defined to be inside or outside the ice region. Finally, the material layup is homogenized at each integration point under the classical laminated plate theory approach based on the defined material properties of the shell, including additional ice in specified regions.

3 Application to wind turbine blades

3.1 NREL/SNL 5 MW Blade Definition

The baseline blade design considered in this study is an NREL/SNL 5 MW blade [109, 110] that has been previously modeled and studied using isogeometric shell analysis [96, 97]. The NURBS-based model of the NREL/SNL 5 MW blade accommodates the discontinuous material regions from the reference design through multiple discrete NURBS surfaces that are connected using a penalty-based patch coupling approach [96], as summarized in Section 2.2. Figure 4 shows the individual blade patches and corresponding layup stacking sequence information for each specific material region. The mesh shown in Figure 4 is the coarsest mesh considered in this work with 10,800 cubic NURBS elements and 16,367 control points. Two additional meshes, which are obtained by one and two additional levels of global h-refinement and denoted as Mesh 2 and Mesh 3, respectively, are also considered in this work. Figure 5 indicates the spanwise thickness distribution of each material stack, and Figure 6 shows the location of each material zone on the airfoil, including an additional ice layer. Further details on the full blade geometry definition and material properties can be found in Herrema et al. [97], which also includes extensive studies of the blade structure, including vibrational and buckling analysis, and an IGA-based blade optimization to reduce the overall cost of energy.

3.2 Ice study geometry and setup

The proposed projection-based ice modeling approach described in Section 2.3 is employed to accurately capture any specified ice shape. This approach provides an effective method to adaptively incorporate variable ice configurations while maintaining the same baseline blade geometry and material definitions. Under this procedure, the defined edge of the ice is projected to the blade surface and used

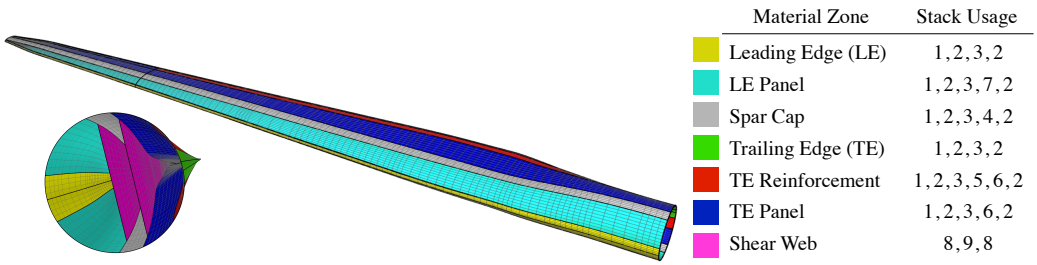

Fig. 4: NREL/SNL 5 MW baseline blade material definition.

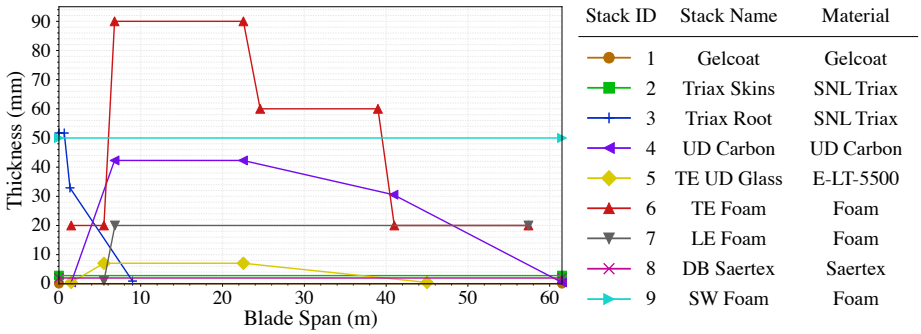

Fig. 5: NREL/SNL 5 MW baseline blade material thickness distributions.

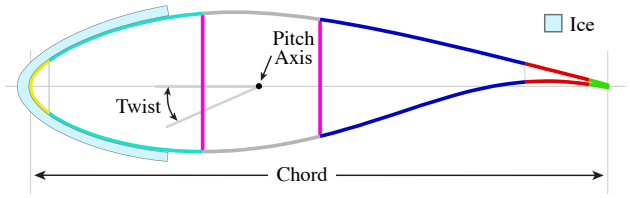

Fig. 6: NREL/SNL 5 MW baseline blade material zones with ice accretion. Colored zones correspond to the legend labels in Figure 4.

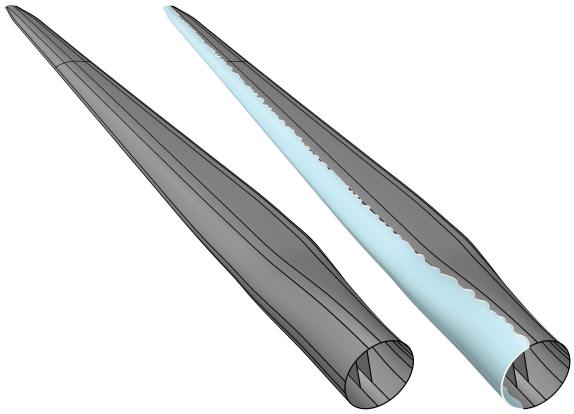

Fig. 7: Baseline blade patches and projected ice shape.

to separate the blade geometry into distinct regions with and without ice accumulation. These areas are determined by splitting the baseline blade into smaller surface subsections using the projected ice edge curve; these subsections are defined to be inside or outside the ice region of the blade based on their relative orientation with respect to the projected ice curve. The corresponding region is indicated for each integration point on the baseline blade surfaces. In this study, an idealized initial ice shape is generated by adding varying degrees of noise to a reference sine wave; however, this approach can be easily adapted to capture realistic ice accretion profiles based on experimental or real-world operational data. Figure 7 shows the baseline blade patches and an example projected ice shape.

The spanwise ice distribution in this study is based on the Germanischer Lloyd (GL) guideline [111] for the mass distribution per unit length that should be considered for blades operating in cold weather conditions. This is a typical design standard that is defined as a linearly increasing mass distribution from zero to a value of μ_{ice} between the root and half the rotor radius and as a constant distribution for the remaining rotor span. In this guideline, μ_{ice} is the mass distribution per unit length of ice on the leading edge of the rotor blade, which is defined as

$$\mu_{\text{ice}} = \rho_{\text{ice}}\, k\, c_{\text{min}}(c_{\text{max}} + c_{\text{min}}), \tag{17}$$

where

$$k = 0.00675 + 0.3e^{-0.32R/R_1} \tag{18}$$

is an empirically defined scaling constant, ρ_{ice} is the density of ice, R is the rotor radius, $R_1 = 1$ m is the unit radius, c_{max}

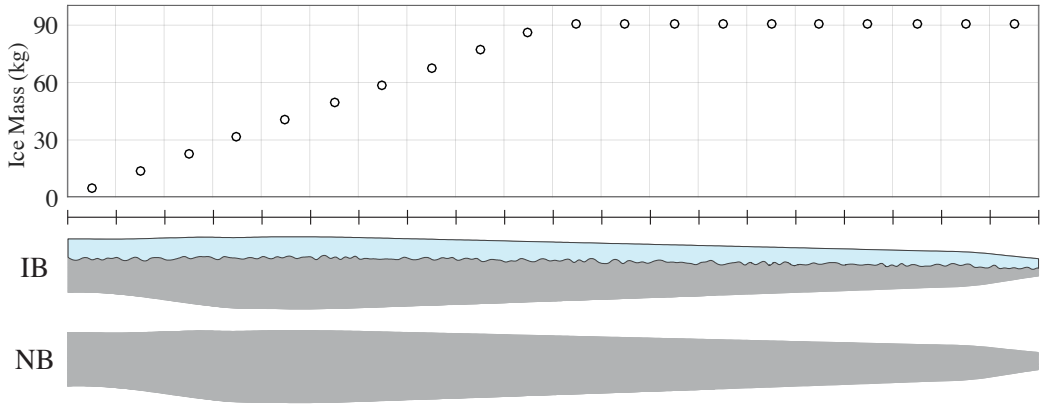

Fig. 8: Ice mass of each span region in relation to the NREL/SNL 5 MW with the baseline ice configuration (IB). The blade with no ice (NB) is also shown for reference. The thickness of ice in each region of the IB configuration is below 30 mm.

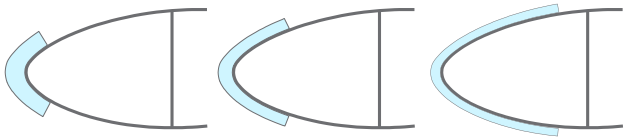

Fig. 9: Example of differing ice thickness distributions based on defined mass distribution and ice region areas.

is the maximum chord length, and $c_{\min}$ is the chord length at the blade tip. Length and mass quantities are defined in meters and kilograms, respectively. In order to simply transfer this standard mass distribution into a thickness distribution for shell analysis, this study identifies blade span sections, as indicated in Figure 8, and assumes a constant thickness within each section. The ice is defined as an isotropic, elastic material with a Young's modulus of 10 GPa, Poisson's ratio of 0.3, and a density of 700 kg/m^3 [108, 111, 112].

Although this design standard considers the impact of added ice mass on the blade, it does not specify the chordwise or spanwise ice distributions. As a result, the structural behavior of the blade may vary significantly depending which type of ice profile is considered. This work proposes a study of seven different ice configurations to determine the impact of differing types of ice accretion on the structural behavior of the NREL/SNL 5 MW blade. Figure 8 shows the total ice mass within each defined section along the blade span, which remains unchanged for each ice configuration. The corresponding thickness is defined for each span section based on the total area of ice within each section. As shown schematically in Figure 9, the effect of considering this generalized mass distribution corresponds to thickness distributions for which smaller ice sections have thicker ice accumulation. We note that the thickness of the added layer of ice in each region is below 100 mm for all the cases considered in this work, which maintains the thin-shell approximation for this problem. To determine the structural effect of

Table 1: Analytical NURBS surface area for the baseline ice shape (IB) compared to the computed numerical ice area for the baseline ice shape for each blade mesh level.

	Area (m^2)	Diff. (%)
NURBS	171.79	—
Mesh 1	171.88	5.14×10^{-2}
Mesh 2	171.73	-3.43×10^{-2}
Mesh 3	171.78	-4.59×10^{-3}

ice accretion, the baseline ice accretion case (IB) is initially compared to the NREL/SNL 5 MW blade with no ice (NB), which are both shown in Figure 8. In addition, two different types of ice configurations are considered in this work and compared to the baseline ice configuration (IB). Two cases of ice accretion at different locations from the leading edge (L1 and L2) are generated to determine the impact of shifting the ice formation (Figure 10). Four cases with different degrees of noise in the ice shape (A0–A3) are also investigated to determine the structural impact of ice shape variation (Figure 11).

The performance of this projection-based ice modeling approach relies on the convergence of the projected ice area. In practice, this depends on how accurately the projected geometry is captured by the surface integration points. Table 1 shows the analytical area of the NURBS surface compared to the numerically integrated area of the baseline projected ice shape on each blade mesh. These quantities demonstrate overall convergence of the projected ice shape under mesh refinement.

3.3 Vibrational analysis

The vibration behavior of wind turbine blades is an important structural design quantity that can be significantly im-

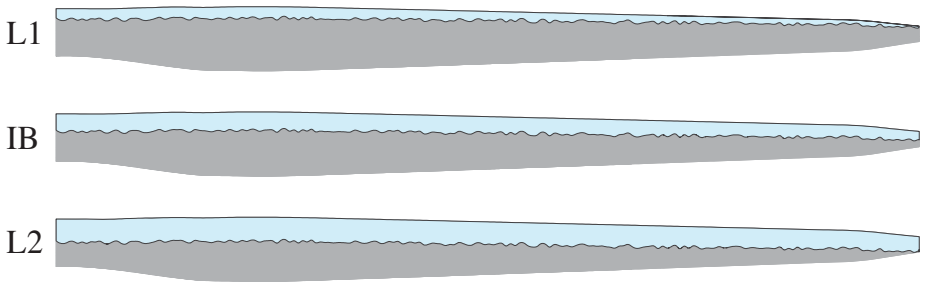

Fig. 10: Ice accretion cases at varying location.

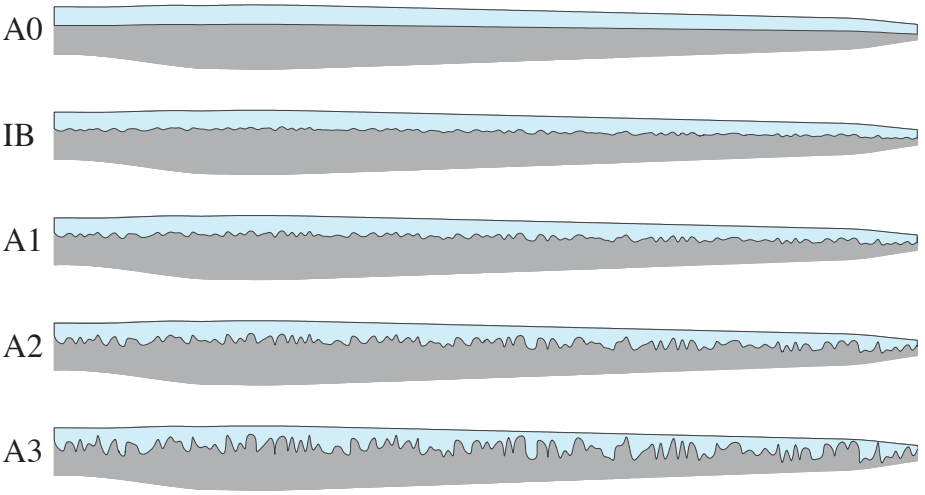

Fig. 11: Ice accretion with varying degrees of profile noise.

pacted by ice accretion. The reference NREL/SNL 5 MW blade is designed so that the natural frequencies of vibration will not coincide with the typical frequencies that occur during the normal operation of the turbine. With the additional mass and stiffness introduced by a layer of ice in certain regions of the blade, the natural frequencies will change accordingly. The linear vibration analysis is performed by considering the following eigenvalue problem:

$$\left(\mathbf{K}^{\text{lin}} - \lambda_i \mathbf{M}\right) \mathbf{v}_i = 0 \,, \tag{19}$$

where $\mathbf{K}^{\text{lin}}$ is the linear stiffness matrix of the structure, $\mathbf{M}$ is the mass matrix, and λ_i is the i^{th} eigenvalue associated with mode vector $\mathbf{v}_i$. The relationship between the i^{th} frequency of vibration, ω_i, and the eigenvalue is given by the equation $\omega_i^2 = \lambda_i$. The eigenvalue problem is solved using SLEPc [113, 114], which is a scientific package within the PETSc software package [115].

To investigate the impact of blade refinement on the icing analysis, a refinement study is performed for the frequency analysis of the baseline ice shape. As shown in Table 2, the blade frequencies are analyzed for each mesh refinement level and indicate overall convergence under mesh refinement. The results from this study indicate less than 0.05% difference between Mesh 2 and Mesh 3 for each frequency. Based on these results and the ice area convergence study presented in Section 3.2, Mesh 2 is selected for all following ice accretion studies.

Table 2: Vibrational analysis results from the NREL/SNL 5 MW blade with a baseline ice configuration (IB) for each level of mesh refinement.

Frequency (Hz)	Mesh 1	Mesh 2	Mesh 3
1st flapwise	0.8172	0.8171	0.8171
1st edgewise	0.9780	0.9774	0.9773
2nd flapwise	2.5818	2.5807	2.5803
2nd edgewise	3.7807	3.7786	3.7780
3rd flapwise	5.4550	5.4499	5.4480
1st torsion	6.9743	6.9664	6.9633

The vibrational analysis results from the NREL/SNL 5 MW blade with no ice and the iced blade for the baseline ice configuration (Figure 8) on Mesh 2 are shown in Table 3. These quantities indicate a significant change in blade frequencies due to the increased mass and stiffness of the blade under icing conditions. Overall, the lowest bending modes

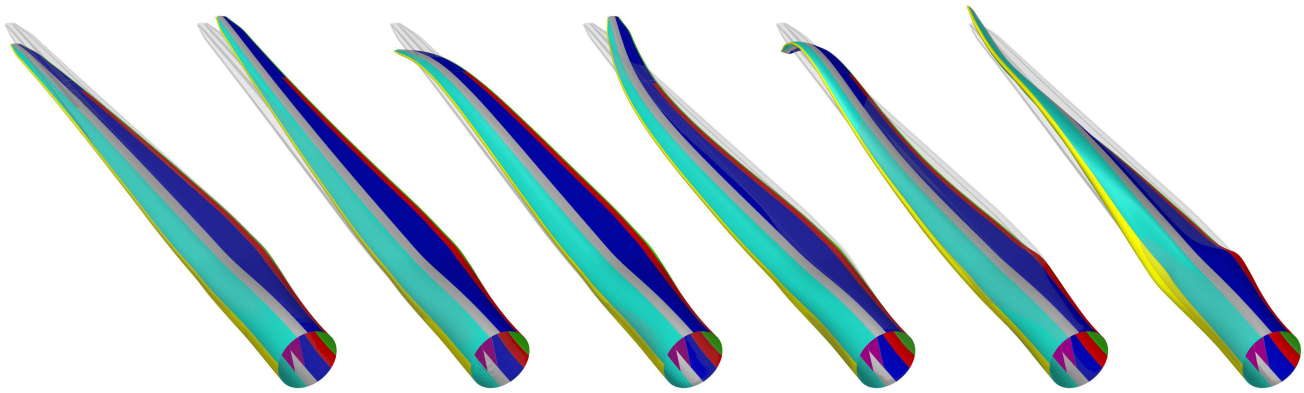

Fig. 12: Mode shapes for the baseline ice configuration (IB) are superimposed with the reference undeformed configuration. Mode shapes are ordered from left to right: 1st flapwise, 1st edgewise, 2nd flapwise, 2nd edgewise, 3rd flapwise, and 1st torsion.

Table 3: Vibrational analysis results from NREL/SNL 5 MW blade with no ice (NB) and the iced blade with baseline ice configuration (IB).

Frequency	NB (Hz)	IB (Hz)	Diff. (%)
1st flapwise	0.9194	0.8170	−11.131
1st edgewise	1.0552	0.9774	−7.380
2nd flapwise	2.8106	2.5807	−8.182
2nd edgewise	3.8870	3.7786	−2.789
3rd flapwise	5.6904	5.4498	−4.226
1st torsion	6.7152	6.9663	3.739

exhibit the largest decreases in eigenfrequency, while the higher modes exhibit more moderate changes in frequency, with the torsion mode showing an increase. These changes in the natural frequencies of the blade may introduce a number of potential issues for wind turbine operation under icing conditions, including a higher potential for the natural frequencies of the blade to be excited by the other turbine frequencies, such as the rotor frequency. Figure 12 shows the mode shapes for the baseline ice configuration (IB) compared to the undeformed blade configuration.

The effect of different ice configurations is also examined for each case outlined in Section 3.2 (Figures 10 and 11) and compared to the baseline ice case. As shown in Figure 13a, the change in ice location induces clear variation in the blade frequencies. Comparisons between the edgewise and flapwise modes exhibit a noticeable trend, with higher modes generating more deviation from the baseline case. The L1 case also exhibits higher overall frequency deviation compared to the L2 case. As shown in Figure 13b, changes in the ice shape profile induce less pronounced frequency changes. Compared to the baseline, changes in the degree of noise in the ice profile produce less than 1% difference for all the cases. Overall, the edgewise frequencies demonstrate higher differences than the flapwise frequencies, and the highest degree of noise exhibits the largest change from the baseline.

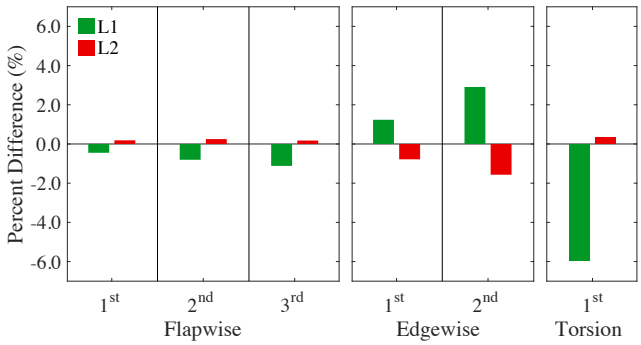

(a) Ice accretion at varying locations.

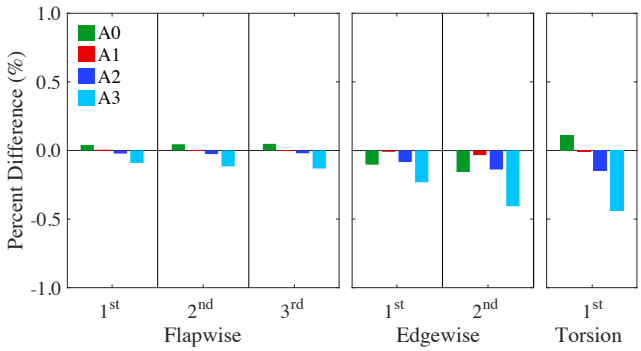

(b) Ice accretion with varying degrees of profile noise.

Fig. 13: Vibrational analysis results compared to the baseline ice configuration (IB).

3.4 Nonlinear deflection analysis

The maximum tip deflection of the NREL/SNL 5 MW wind turbine blade is another important structural performance metric. Particularly with the development of more flexible

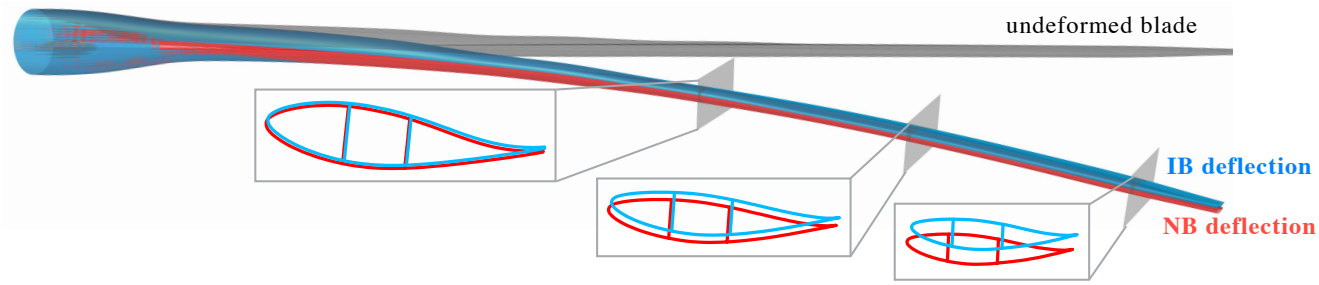

Fig. 14: Blade deflection of the NREL/SNL 5 MW blade with no ice (NB) compared to the baseline ice configuration (IB) shown in red and blue, respectively. Airfoil cross sections in the deformed configuration are extracted from the 38 m, 48 m, and 58 m span locations in the undeformed configuration.

blades, the deflection should be appropriately considered to avoid clearance issues between the rotor and the tower and to ensure proper operating conditions for pre-bent blades, especially considering the impact of ice. The NREL/SNL 5 MW blade is simulated under a 50-year extreme wind condition with 70 m/s winds, a fixed rotor, blades feathered to 90°, and 15° of yaw misalignment, as specified by design load case (DLC) 6.1 in the IEC 61400 design standard [116]. The aerodynamic loads at the time instance with the largest blade root bending moment in the flapwise direction are collected from NREL's FAST [117] and applied to the IGA-based blade analysis, as described in Herrema et al. [96]. Since the orientation of this blade is arbitrary, the gravitational effect on the blade is neglected for this analysis.

Table 4 shows the maximum tip displacement for each ice configuration compared to the NREL/SNL 5 MW blade with no ice. In each case, the added ice induces a decrease in the maximum tip deflection, with the L1 and L2 cases exhibiting the smallest and largest decreases, respectively. This likely results from increasing the stiffness in larger areas of the blade, which also demonstrates why the same mass distribution along the blade can induce different degrees of change in deflection depending on the chordwise distribution of ice on the blade. Variations in the ice shape profile again induce less pronounced changes in the quantity of interest, with all deflection changes due to the ice shape profile falling within 0.02 m. Figure 14 shows the total deflection of the NREL/SNL 5 MW blade with no ice compared to the baseline ice configuration.

Table 4: Magnitude of the maximum tip deflection of the NREL/SNL 5 MW blade with no ice (NB) compared to each icing configuration.

	Tip Displacement	
Case	Magnitude (m)	Diff. (%)
NB	6.7088	—
IB	6.4569	−3.755
L1	6.5607	−2.208
L2	6.4217	−4.279
A0	6.4515	−3.836
A1	6.4575	−3.746
A2	6.4586	−3.729
A3	6.4650	−3.634

4 Conclusion

This study presents a novel approach to include ice accretion in isogeometric shell analysis of complex structures. The proposed methodology utilizes the advantages of IGA to develop a combined geometry modeling and analysis procedure that is effective for simulating wind turbine blades with ice accretion. This integrated projection-based IGA approach directly incorporates the existing CAD model and material definitions and eliminates time-consuming geometry manipulation and meshing steps that are necessary for more typical high-fidelity analysis methods.

The significant change in vibrational frequencies and maximum tip deflections demonstrated by this study indicate the need for testing and accommodation for turbines operating in cold weather conditions. Current design standards are very broad in terms of the type of ice accretion that is considered. Mass distributions standards alone do not properly account for the significant variation that may be present on wind turbine blades that operate under icing conditions. As this study demonstrates, geometric variation in ice accretion can have a significant impact on the vibrational modes and deflection of wind turbine blades. Further high-fidelity analysis of this effect, especially considering realistic ice distributions, is necessary to design reliable turbines that can operate effectively in cold climates. Changes in the vibrational behavior of these blades also heavily impact the dynamic performance of these structures and may induce significant additional loads and fatigue on the blade. Variations in the degree of ice accretion on individual blades may also introduce imbalances in the structural loading on

the rotor that can contribute to unexpected fatigue. Future studies of these phenomena could inform improved design standards and safety factors for icing conditions and could help reduce operation and maintenance costs and downtime for turbines in colder climates. Overall, such improved standards would decrease the cost of energy and establish wind energy as an even more competitive form of renewable energy generation.

Although the IGA methods in this study have been thoroughly validated, specifically the methods for shell analysis of multilayer materials, additional validation of the ice modeling approaches would further demonstrate the utility of these methods for simulating realistic ice accretion. In the future, these methods could also be used to study a variety of different icing phenomena and their impact on the blade behavior and performance, including the blade dynamics and fatigue properties under icing conditions. Further studies on the impact of different types of ice accretion, including varying thickness distributions in the spanwise and chordwise directions on the blade, asymmetric ice distributions on the pressure and suction sides of the blade, and different types of ice configurations, could be performed in the future to comprehensively analyze the impact of ice accretion using the high-fidelity analysis methods outlined in this work.

Acknowledgments

E.L. Johnson was partially supported by the U.S. National Science Foundation (NSF) Grant No. DGE-1069283 which funds the activities of the Integrative Graduate Education and Research Traineeship (IGERT) in Wind Energy Science, Engineering, and Policy (WESEP) at Iowa State University. This support is gratefully acknowledged.

References

1. D. J. Sailor, M. Smith, and M. Hart. Climate change implications for wind power resources in the Northwest United States. *Renewable Energy*, 33:2393–2406, 2008.
2. L. Battisti. *Wind Turbines in Cold Climates: Icing Impacts and Mitigation Systems*. Springer International Publishing, Switzerland, 2015.
3. W. J. Jasinski, S. C. Noe, M. S. Selig, and M. B. Bragg. Wind turbine performance under icing conditions. *Journal of Solar Energy Engineering*, 120:60–65, 1998.
4. C. Hochart, G. Fortin, J. Perron, and A. Ilinca. Wind turbine performance under icing conditions. *Wind Energy*, 11:319–333, 2008.
5. M. S. Virk, M. C. Homola, and P. J. Nicklasson. Relation between angle of attack and atmospheric ice accretion on large wind turbine's blade. *Wind Engineering*, 34(6):607–613, 2010.
6. M. S. Virk, M. C. Homola, and P. J. Nicklasson. Effect of rime ice accretion on aerodynamic characteristics of wind turbine blade profiles. *Wind Engineering*, 34(2):207–218, 2010.
7. S. Barber, Y. Wang, S. Jafari, N. Chokani, and R. S. Abhari. The impact of ice formation on wind turbine performance and aerodynamics. *Journal of Solar Energy Engineering*, 133:011007, 2011.
8. P. J. Nicklasson M. C. Homola, M. S. Virk and P. A. Sundsbø. Performance losses due to ice accretion for a 5 MW wind turbine. *Wind Energy*, 15:379–389, 2012.
9. A. Hudecz, H. Koss, and M. O. L. Hansen. Ice accretion on wind turbine blades. In *15th International workshop on atmospheric icing of structures (IWAIS XV)*, St. John's, Canada, 2013.
10. M. Etemaddar, M. O. L. Hansen, and T. Moan. Wind turbine aerodynamic response under atmospheric icing conditions. *Wind Energy*, 17(2):241–265, 2014.
11. O. Yirtici, I. H. Tuncer, and S. Ozgen. Ice accretion prediction on wind turbines and consequent power losses. *Journal of Physics: Conference Series*, 753:022022, 2016.
12. P. Blasco, J. Palacios, and S. Schmitz. Effect of icing roughness on wind turbine power production. *Wind Energy*, 20(4):601–617, 2017.
13. L. Gao, Y. Liu, W. Zhou, and H. Hu. An experimental study on the aerodynamic performance degradation of a wind turbine blade model induced by ice accretion process. *Renewable Energy*, 133:663–675, 2019.
14. O. Yirtici, S. Ozgen, and I. H. Tuncer. Predictions of ice formations on wind turbine blades and power production losses due to icing. *Wind Energy*, 22(7):945–958, 2019.
15. L. Gao, Y. Liu, and H. Hu. An experimental investigation of dynamic ice accretion process on a wind turbine airfoil model considering various icing conditions. *International Journal of Heat and Mass Transfer*, 133:930–939, 2019.
16. L. Gao, R. Veerakumar, Y. Liu, and H. Hu. Quantification of the 3D shapes of the ice structures accreted on a wind turbine airfoil model. *Journal of Visualization*, 22:661–667, 2019.
17. A. S. Y. Alsabagh, W. Tiu, Y. Xu, and M. S. Virk. A review of the effects of ice accretion on the structural behavior of wind turbines. *Wind Engineering*, 37:59–70, 2013.
18. S. Gantasala, J.-C. Luneno, and J.-O. Aidanpää. Identification of ice mass accumulated on wind turbine blades using its natural frequencies. *Wind Engineering*, 42:66–84, 2018.
19. A. S. Y. Alsabagh, Y. Xu, M. S. Virk, and O. Badran. Atmospheric ice loading and its impact on natural frequencies of wind turbines. *Wind Engineering*, 39:83–96, 2015.
20. S. Gantasala, J.-C. Luneno, and J.-O. Aidanpää. Influence of icing on the modal behavior of wind turbine blades. *Energies*, 9:862, 2016.
21. S. Gantasala, N. Tabatabaei, M. Cervantes, and J.-O. Aidanpää. Numerical investigation of the aeroelastic behavior of a wind turbine with iced blades. *Energies*, 12(12):2422, 2019.
22. T. J. R. Hughes, J. A. Cottrell, and Y. Bazilevs. Isogeometric analysis: CAD, finite elements, NURBS, exact geometry and mesh refinement. *Computer Methods in Applied Mechanics and Engineering*, 194:4135–4195, 2005.
23. G. Lorenzo, M. A. Scott, K. Tew, T. J. R. Hughes, Y. Zhang, L. Liu, G. Vilanova, and H. Gomez. Tissue-scale, personalized modeling and simulation of prostate cancer growth. *Proceedings of the National Academy of Sciences*, 113(48):E7663–E7671, 2016.
24. K. Takizawa, T. E. Tezduyar, and T. Terahara. Ram-air parachute structural and fluid mechanics computations with the space–time isogeometric analysis (ST-IGA). *Computers & Fluids*, 141:191–200, 2016.
25. K. Takizawa, T. E. Tezduyar, Y. Otoguro, T. Terahara, T. Kuraishi, and H. Hattori. Turbocharger flow computations with the Space–Time Isogeometric Analysis (ST-IGA). *Computers & Fluids*, 142:15–20, 2017.
26. K. Takizawa, T. E. Tezduyar, and T. Sasaki. Aorta modeling with the element-based zero-stress state and isogeometric discretization. *Computational Mechanics*, 59:265–280, 2017.

27. K. Takizawa, T. E. Tezduyar, T. Terahara, and T. Sasaki. Heart valve flow computation with the integrated Space–Time VMS, Slip Interface, Topology Change and Isogeometric Discretization methods. *Computers & Fluids*, 158:176–188, 2017.
28. Y. Otoguro, K. Takizawa, and T. E. Tezduyar. Space–time VMS computational flow analysis with isogeometric discretization and a general-purpose NURBS mesh generation method. *Computers & Fluids*, 158:189–200, 2017.
29. K. Takizawa, T. E. Tezduyar, and Y. Otoguro. Stabilization and discontinuity-capturing parameters for space–time flow computations with finite element and isogeometric discretizations. *Computational Mechanics*, 62:1169–1186, 2018.
30. Y. Otoguro, K. Takizawa, T. E. Tezduyar, K. Nagaoka, and S. Mei. Turbocharger turbine and exhaust manifold flow computation with the Space–Time Variational Multiscale Method and Isogeometric Analysis. *Computers & Fluids*, 179:764–776, 2019.
31. K. Takizawa, T. E. Tezduyar, H. Uchikawa, T. Terahara, T. Sasaki, and A. Yoshida. Mesh refinement influence and cardiac-cycle flow periodicity in aorta flow analysis with isogeometric discretization. *Computers & Fluids*, 179:790–798, 2019.
32. T. Kanai, K. Takizawa, T. E. Tezduyar, T. Tanaka, and A. Hartmann. Compressible-flow geometric-porosity modeling and spacecraft parachute computation with isogeometric discretization. *Computational Mechanics*, 63:301–321, 2019.
33. T. Kuraishi, K. Takizawa, and T. E. Tezduyar. Space–Time Isogeometric flow analysis with built-in Reynolds-equation limit. *Mathematical Models and Methods in Applied Sciences*, 29:871–904, 2019.
34. Y. Yu, Y. J. Zhang, K. Takizawa, T. E. Tezduyar, and T. Sasaki. Anatomically realistic lumen motion representation in patient-specific space–time isogeometric flow analysis of coronary arteries with time-dependent medical-image data. *Computational Mechanics*, 65:395–404, 2020.
35. Y. Otoguro, K. Takizawa, T. E. Tezduyar, K. Nagaoka, R. Avsar, and Y. Zhang. Space–time VMS flow analysis of a turbocharger turbine with isogeometric discretization: Computations with time-dependent and steady-inflow representations of the intake/exhaust cycle. *Computational Mechanics*, 64:1403–1419, 2019.
36. J. Yan, S. Lin, Y. Bazilevs, and G. J. Wagner. Isogeometric analysis of multi-phase flows with surface tension and with application to dynamics of rising bubbles. *Computers & Fluids*, 179:777–789, 2019.
37. G. Lorenzo, T. J. R. Hughes, P. Dominguez-Frojan, A. Reali, and H. Gomez. Computer simulations suggest that prostate enlargement due to benign prostatic hyperplasia mechanically impedes prostate cancer growth. *Proceedings of the National Academy of Sciences*, 116:1152–1161, 2019.
38. T. Terahara, K. Takizawa, T. E. Tezduyar, A. Tsushima, and K. Shiozaki. Ventricle-valve-aorta flow analysis with the Space–Time Isogeometric Discretization and Topology Change. *Computational Mechanics*, 2020.
39. T. Terahara, K. Takizawa, T. E. Tezduyar, Y. Bazilevs, and M.-C. Hsu. Heart valve isogeometric sequentially-coupled FSI analysis with the space–time topology change method. *Computational Mechanics*, 2020.
40. J. Kiendl, K.-U. Bletzinger, J. Linhard, and R. Wüchner. Isogeometric shell analysis with Kirchhoff–Love elements. *Computer Methods in Applied Mechanics and Engineering*, 198:3902–3914, 2009.
41. D. J. Benson, Y. Bazilevs, M.-C. Hsu, and T. J. R. Hughes. Isogeometric shell analysis: The Reissner–Mindlin shell. *Computer Methods in Applied Mechanics and Engineering*, 199:276–289, 2010.
42. D. J. Benson, Y. Bazilevs, M.-C. Hsu, and T. J. R. Hughes. A large deformation, rotation-free, isogeometric shell. *Computer Methods in Applied Mechanics and Engineering*, 200:1367–1378, 2011.
43. N. Nguyen-Thanh, J. Kiendl, H. Nguyen-Xuan, R. Wüchner, K.U. Bletzinger, Y. Bazilevs, and T. Rabczuk. Rotation-free isogeometric thin shell analysis using PHT-splines. *Computer Methods in Applied Mechanics and Engineering*, 200:3410–3424, 2011.
44. D. J. Benson, S. Hartmann, Y. Bazilevs, M.-C. Hsu, and T. J. R. Hughes. Blended isogeometric shells. *Computer Methods in Applied Mechanics and Engineering*, 255:133–146, 2013.
45. R. Echter, B. Oesterle, and M. Bischoff. A hierarchic family of isogeometric shell finite elements. *Computer Methods in Applied Mechanics and Engineering*, 254:170–180, 2013.
46. Y. Guo and M. Ruess. Nitsche's method for a coupling of isogeometric thin shells and blended shell structures. *Computer Methods in Applied Mechanics and Engineering*, 284:881–905, 2015.
47. J. Kiendl, M.-C. Hsu, M. C. H. Wu, and A. Reali. Isogeometric Kirchhoff–Love shell formulations for general hyperelastic materials. *Computer Methods in Applied Mechanics and Engineering*, 291:280–303, 2015.
48. A. Buganza Tepole, H. Kabaria, K.-U. Bletzinger, and E. Kuhl. Isogeometric Kirchhoff–Love shell formulations for biological membranes. *Computer Methods in Applied Mechanics and Engineering*, 293:328–347, 2015.
49. N. Nguyen-Thanh, N. Valizadeh, M. N. Nguyen, H. Nguyen-Xuan, X. Zhuang, P. Areias, G. Zi, Y. Bazilevs, L. De Lorenzis, and T. Rabczuk. An extended isogeometric thin shell analysis based on Kirchhoff–Love theory. *Computer Methods in Applied Mechanics and Engineering*, 284:265–291, 2015.
50. B. Oesterle, E. Ramm, and M. Bischoff. A shear deformable, rotation-free isogeometric shell formulation. *Computer Methods in Applied Mechanics and Engineering*, 307:235–255, 2016.
51. T. X. Duong, F. Roohbakhshan, and R. A. Sauer. A new rotation-free isogeometric thin shell formulation and a corresponding continuity constraint for patch boundaries. *Computer Methods in Applied Mechanics and Engineering*, 316:43–83, 2017.
52. H. Casquero, L. Liu, Y. Zhang, A. Reali, J. Kiendl, and H. Gomez. Arbitrary-degree T-splines for isogeometric analysis of fully nonlinear Kirchhoff–Love shells. *Computer-Aided Design*, 82:140–153, 2017.
53. F. Roohbakhshan and R. A. Sauer. Efficient isogeometric thin shell formulations for soft biological materials. *Biomechanics and Modeling in Mechanobiology*, 16:1569–1597, 2017.
54. K. Takizawa, T. E. Tezduyar, and T. Sasaki. Isogeometric hyperelastic shell analysis with out-of-plane deformation mapping. *Computational Mechanics*, 63:681–700, 2019.
55. M. C. H. Wu, R. Zakerzadeh, D. Kamensky, J. Kiendl, M. S. Sacks, and M.-C. Hsu. An anisotropic constitutive model for immersogeometric fluid–structure interaction analysis of bioprosthetic heart valves. *Journal of Biomechanics*, 74:23–31, 2018.
56. M. Ambati, J. Kiendl, and L. De Lorenzis. Isogeometric Kirchhoff–Love shell formulation for elasto-plasticity. *Computer Methods in Applied Mechanics and Engineering*, 340:320–339, 2018.
57. N. Liu, X. Ren, and J. Lua. An isogeometric continuum shell element for modeling the nonlinear response of functionally graded material structures. *Composite Structures*, 237:111893, 2020.
58. D. J. Benson, Y. Bazilevs, E. De Luycker, M.-C. Hsu, M. Scott, T. J. R. Hughes, and T. Belytschko. A generalized finite element formulation for arbitrary basis functions: from isogeometric analysis to XFEM. *International Journal for Numerical Methods in Engineering*, 83:765–785, 2010.
59. J. Kiendl, Y. Bazilevs, M.-C. Hsu, R. Wüchner, and K.-U. Bletzinger. The bending strip method for isogeometric analysis of Kirchhoff–Love shell structures comprised of multiple patches. *Computer Methods in Applied Mechanics and Engineering*, 199:2403–2416, 2010.

60. M.-C. Hsu, D. Kamensky, Y. Bazilevs, M. S. Sacks, and T. J. R. Hughes. Fluid–structure interaction analysis of bioprosthetic heart valves: significance of arterial wall deformation. *Computational Mechanics*, 54:1055–1071, 2014.
61. M. Breitenberger, A. Apostolatos, B. Philipp, R. Wüchner, and K.-U. Bletzinger. Analysis in computer aided design: Nonlinear isogeometric B-Rep analysis of shell structures. *Computer Methods in Applied Mechanics and Engineering*, 284:401–457, 2015.
62. Y. Guo and M. Ruess. Weak Dirichlet boundary conditions for trimmed thin isogeometric shells. *Computers and Mathematics with Applications*, 70:1425–1440, 2015.
63. D. Kamensky, M.-C. Hsu, D. Schillinger, J. A. Evans, A. Aggarwal, Y. Bazilevs, M. S. Sacks, and T. J. R. Hughes. An immersogeometric variational framework for fluid–structure interaction: Application to bioprosthetic heart valves. *Computer Methods in Applied Mechanics and Engineering*, 284:1005–1053, 2015.
64. M.-C. Hsu, D. Kamensky, F. Xu, J. Kiendl, C. Wang, M. C. H. Wu, J. Mineroff, A. Reali, Y. Bazilevs, and M. S. Sacks. Dynamic and fluid–structure interaction simulations of bioprosthetic heart valves using parametric design with T-splines and Fung-type material models. *Computational Mechanics*, 55:1211–1225, 2015.
65. M.-C. Hsu, C. Wang, A. J. Herrema, D. Schillinger, A. Ghoshal, and Y. Bazilevs. An interactive geometry modeling and parametric design platform for isogeometric analysis. *Computers and Mathematics with Applications*, 70:1481–1500, 2015.
66. J. Yan, B. Augier, A. Korobenko, J Czarnowski, G Ketterman, and Y. Bazilevs. FSI modeling of a propulsion system based on compliant hydrofoils in a tandem configuration. *Computers & Fluids*, 141:201–211, 2016.
67. Y. Guo, M. Ruess, and D. Schillinger. A parameter-free variational coupling approach for trimmed isogeometric thin shells. *Computational Mechanics*, 59:693–715, 2016.
68. X. Zhang, C. Jin, P. Hu, X. Zhu, W. Hou, J. Xu, C. Wang, Y. Zhang, Z.-D. Ma, and H. Smith. NURBS modeling and isogeometric shell analysis for complex tubular engineering structures. *Computational and Applied Mathematics*, 36:1659–1679, 2016.
69. J. Kiendl, M. Ambati, L. De Lorenzis, H. Gomez, and A. Reali. Phase-field description of brittle fracture in plates and shells. *Computer Methods in Applied Mechanics and Engineering*, 312:374–394, 2016.
70. C. Wang, M. C. H. Wu, F. Xu, M.-C. Hsu, and Y. Bazilevs. Modeling of a hydraulic arresting gear using fluid–structure interaction and isogeometric analysis. *Computers & Fluids*, 142:3–14, 2017.
71. M. C. H. Wu, D. Kamensky, C. Wang, A. J. Herrema, F. Xu, M. S. Pigazzini, A. Verma, A. L. Marsden, Y. Bazilevs, and M.-C. Hsu. Optimizing fluid–structure interaction systems with immersogeometric analysis and surrogate modeling: Application to a hydraulic arresting gear. *Computer Methods in Applied Mechanics and Engineering*, 316:668–693, 2017.
72. L. Heltai, J. Kiendl, A. DeSimone, and A. Reali. A natural framework for isogeometric fluid–structure interaction based on BEM–shell coupling. *Computer Methods in Applied Mechanics and Engineering*, 316:522–546, 2017.
73. Y. Guo, J. Heller, T. J. R. Hughes, M. Ruess, and D. Schillinger. Variationally consistent isogeometric analysis of trimmed thin shells at finite deformations, based on the STEP exchange format. *Computer Methods in Applied Mechanics and Engineering*, 336:39–79, 2018.
74. F. Xu, S. Morganti, R. Zakerzadeh, D. Kamensky, F. Auricchio, A. Reali, T. J. R. Hughes, M. S. Sacks, and M.-C. Hsu. A framework for designing patient-specific bioprosthetic heart valves using immersogeometric fluid–structure interaction analysis. *International Journal for Numerical Methods in Biomedical Engineering*, 34:e2938, 2018.
75. D. Kamensky, F. Xu, C.-H. Lee, J. Yan, Y. Bazilevs, and M.-C. Hsu. A contact formulation based on a volumetric potential: Application to isogeometric simulations of atrioventricular valves. *Computer Methods in Applied Mechanics and Engineering*, 330:522–546, 2018.
76. T. Teschemacher, A. M. Bauer, T. Oberbichler, M. Breitenberger, R. Rossi, R. Wüchner, and K.-U. Bletzinger. Realization of CAD-integrated shell simulation based on isogeometric B-Rep analysis. *Advanced Modeling and Simulation in Engineering Sciences*, 5:19, 2018.
77. M. C. H. Wu, H. M. Muchowski, E. L. Johnson, M. R. Rajanna, and M.-C. Hsu. Immersogeometric fluid–structure interaction modeling and simulation of transcatheter aortic valve replacement. *Computer Methods in Applied Mechanics and Engineering*, 357:112556, 2019.
78. A. Balu, S. Nallagonda, F. Xu, A. Krishnamurthy, M.-C. Hsu, and S. Sarkar. A deep learning framework for design and analysis of surgical bioprosthetic heart valves. *Scientific Reports*, 9:18560, 2019.
79. Y. Guo, H. Do, and M. Ruess. Isogeometric stability analysis of thin shells: From simple geometries to engineering models. *International Journal for Numerical Methods in Engineering*, 118:433–458, 2019.
80. L. F. Leidinger, M. Breitenberger, A. M. Bauer, S. Hartmann, R. Wüchner, K.-U. Bletzinger, F. Duddeck, and L. Song. Explicit dynamic isogeometric B-Rep analysis of penalty-coupled trimmed NURBS shells. *Computer Methods in Applied Mechanics and Engineering*, 351:891–927, 2019.
81. H. Casquero, X. Wei, D. Toshniwal, A. Li, T. J. R. Hughes, J. Kiendl, and Y. Zhang. Seamless integration of design and Kirchhoff–Love shell analysis using analysis-suitable unstructured T-splines. *Computer Methods in Applied Mechanics and Engineering*, 360:112765, 2020.
82. A. Nitti, J. Kiendl, A. Reali, and M. D. de Tullio. An immersed-boundary/isogeometric method for fluid–structure interaction involving thin shells. *Computer Methods in Applied Mechanics and Engineering*, 364:112977, 2020.
83. Y. Bazilevs, M.-C. Hsu, J. Kiendl, R. Wüchner, and K.-U. Bletzinger. 3D simulation of wind turbine rotors at full scale. Part II: Fluid–structure interaction modeling with composite blades. *International Journal for Numerical Methods in Fluids*, 65:236–253, 2011.
84. X. Deng, A. Korobenko, J. Yan, and Y. Bazilevs. Isogeometric analysis of continuum damage in rotation-free composite shells. *Computer Methods in Applied Mechanics and Engineering*, 284:349–372, 2015.
85. Y. Bazilevs, M. S. Pigazzini, A Ellison, and H. Kim. A new multi-layer approach for progressive damage simulation in composite laminates based on isogeometric analysis and Kirchhoff-Love shells. Part I: basic theory and modeling of delamination and transverse shear. *Computational Mechanics*, 62:563–585, 2018.
86. M. S. Pigazzini, Y. Bazilevs, A Ellison, and H. Kim. A new multi-layer approach for progressive damage simulation in composite laminates based on isogeometric analysis and Kirchhoff-Love shells. Part II: impact modeling. *Computational Mechanics*, 62:587–601, 2018.
87. M. S. Pigazzini, Y. Bazilevs, A. Ellison, and H. Kim. Isogeometric analysis for simulation of progressive damage in composite laminates. *Journal of Composite Materials*, 52:3471–3489, 2018.
88. M. S. Pigazzini, D. Kamensky, D. A. P. van Iersel, M. D. Alaydin, J. J. C. Remmers, and Y. Bazilevs. Gradient-enhanced damage modeling in Kirchhoff–Love shells: Application to isogeometric analysis of composite laminates. *Computer Methods in Applied Mechanics and Engineering*, 346:152–179, 2019.

89. C. H. Thai, H. Nguyen-Xuan, N. Nguyen-Thanh, T.-H. Le, T. Nguyen-Thoi, and T. Rabczuk. Static, free vibration, and buckling analysis of laminated composite Reissner-Mindlin plates using NURBS-based isogeometric approach. *International Journal for Numerical Methods in Engineering*, 91:571–603, 2012.
90. C. H. Thai, A. J. M. Ferreira, E. Carrera, and H. Nguyen-Xuan. Isogeometric analysis of laminated composite and sandwich plates using a layerwise deformation theory. *Composite Structures*, 104:196–214, 2013.
91. Y. Guo and M. Ruess. A layerwise isogeometric approach for NURBS-derived laminate composite shells. *Composite Structures*, 124:300–309, 2015.
92. N. Liu and A. E. Jeffers. Isogeometric analysis of laminated composite and functionally graded sandwich plates based on a layerwise displacement theory. *Composite Structures*, 176:143–153, 2017.
93. Y. Bazilevs, M.-C. Hsu, J. Kiendl, and D. J. Benson. A computational procedure for prebending of wind turbine blades. *International Journal for Numerical Methods in Engineering*, 89:323–336, 2012.
94. A. Korobenko, M.-C. Hsu, I. Akkerman, J. Tippmann, and Y. Bazilevs. Structural mechanics modeling and FSI simulation of wind turbines. *Mathematical Models and Methods in Applied Sciences*, 23:249–272, 2013.
95. Y. Bazilevs, X. Deng, A. Korobenko, F. Lanza di Scalea, M. D. Todd, and S. G. Taylor. Isogeometric fatigue damage prediction in large-scale composite structures driven by dynamic sensor data. *Journal of Applied Mechanics*, 82:091008, 2015.
96. A. J. Herrema, E. L. Johnson, D. Proserpio, M. C. H. Wu, J. Kiendl, and M.-C. Hsu. Penalty coupling of non-matching isogeometric Kirchhoff–Love shell patches with application to composite wind turbine blades. *Computer Methods in Applied Mechanics and Engineering*, 346:810–840, 2019.
97. A. J. Herrema, J. Kiendl, and M.-C. Hsu. A framework for isogeometric-analysis-based optimization of wind turbine blade structures. *Wind Energy*, 22:153–170, 2019.
98. Y. Bazilevs, M.-C. Hsu, and M. A. Scott. Isogeometric fluid–structure interaction analysis with emphasis on non-matching discretizations, and with application to wind turbines. *Computer Methods in Applied Mechanics and Engineering*, 249–252:28–41, 2012.
99. M.-C. Hsu and Y. Bazilevs. Fluid–structure interaction modeling of wind turbines: simulating the full machine. *Computational Mechanics*, 50:821–833, 2012.
100. Y. Bazilevs, K. Takizawa, T. E. Tezduyar, M.-C. Hsu, N. Kostov, and S. McIntyre. Aerodynamic and FSI analysis of wind turbines with the ALE-VMS and ST-VMS methods. *Archives of Computational Methods in Engineering*, 21:359–398, 2014.
101. Y. Bazilevs, A. Korobenko, X. Deng, and J. Yan. Novel structural modeling and mesh moving techniques for advanced fluid–structure interaction simulation of wind turbines. *International Journal for Numerical Methods in Engineering*, 102:766–783, 2014.
102. J. Yan, A. Korobenko, X. Deng, and Y. Bazilevs. Computational free-surface fluid–structure interaction with application to floating offshore wind turbines. *Computers & Fluids*, 141:155–174, 2016.
103. Y. Bazilevs, A. Korobenko, X. Deng, and J. Yan. Fluid-structure interaction modeling for fatigue-damage prediction in full-scale wind-turbine blades. *Journal of Applied Mechanics*, 83:061010, 2016.
104. A. Korobenko, J. Yan, S. M. I. Gohari, S. Sarkar, and Y. Bazilevs. FSI simulation of two back-to-back wind turbines in atmospheric boundary layer flow. *Computers & Fluids*, 158:167–175, 2017.
105. Y. Bazilevs, J. Yan, X. Deng, and A. Korobenko. Computer modeling of wind turbines: 2. Free-surface FSI and fatigue-damage. *Archives of Computational Methods in Engineering*, 26:1101–1115, 2018.
106. J. N. Reddy. *Mechanics of Laminated Composite Plates and Shells: Theory and Analysis, 2nd ed.* CRC Press, Boca Raton, FL, 2004.
107. J. Kiendl. *Isogeometric Analysis and Shape Optimal Design of Shell Structures*. PhD thesis, Lehrstuhl für Statik, Technische Universität München, 2011.
108. L.W. Gold. On the elasticity of ice plates. *Canadian Journal of Civil Engineering*, 15:1080–1084, 1988.
109. J. Jonkman, S. Butterfield, W. Musial, and G. Scott. Definition of a 5-MW reference wind turbine for offshore system development. Technical Report NREL/TP-500-38060, National Renewable Energy Laboratory, 2009.
110. B. R. Resor. Definition of a 5MW/61.5m wind turbine blade reference model. Technical Report SAND2013-2569, Sandia National Laboratories, Albuquerque, NM, 2013.
111. Germanischer Lloyd Hamburg. Guideline for the Certification of Wind Turbines. Technical report, Germanischer Lloyd Industrial Services GmbH, Hamburg, Germany, 2010.
112. J. M. Krishnan, A. P. Deshpande, and P. B. S. Kumar. *Rheology of Complex Fluids*. Springer, New York, NY, 2010.
113. V. Hernandez, J. E. Roman, and V. Vidal. SLEPc: A scalable and flexible toolkit for the solution of eigenvalue problems. *ACM Transactions on Mathematical Software*, 31:351–362, 2005.
114. J. E. Roman, C. Campos, E. Romero, and A. Tomas. SLEPc users manual. Technical Report DSIC-II/24/02 - Revision 3.7, D. Sistemes Informàtics i Computació, Universitat Politècnica de València, Valencia, Spain, 2016.
115. S. Balay, W. Gropp, L. C. McInnes, and B. Smith. PETSc 2.0 users manual. Mathematics and Computer Science Division, Argonne National Laboratory. http://www.mcs.anl.gov/petsc, 2000.
116. International Electrotechnical Commission. International Standard IEC 61400-1. Wind turbines–Part 1: Design requirements. Geneva, Switzerland, 2005.
117. J. M. Jonkman and M. L. Buhl Jr. FAST user's guide. Technical Report NREL/EL-500-38230, National Renewable Energy Laboratory, Golden, CO, 2005.